Ceramics International 50 (2024) 6017–6024

Contents lists available at ScienceDirect

Ceramics International

journal homepage: www.elsevier.com/locate/ceramint

# Microstructure evolution and mechanical behavior of magnetron sputtering AlN–Al nanostructured composite film

Bingyang Ma [a], Boyuan Sun [a], Hailong Shang [a,*], Rongbin Li [a], Haoxin Cao [a], Filipe Fernandes [b,c]

[a] School of Materials Science, Shanghai Dianji University, Shanghai, 200240, PR China
[b] University of Coimbra, CEMMPRE, ARISE, Department of Mechanical Engineering, Rua Luís Reis Santos, 3030-788, Coimbra, Portugal
[c] ISEP, Polytechnic of Porto, Rua Dr. António Bernardino de Almeida, 4249-015, Porto, Portugal

ARTICLE INFO

Handling Editor: Dr P. Vincenzini

*Keywords:*
Reactive magnetron sputtering
AlN–Al film
Nanocomposite structure
Mechanical properties
Toughening

ABSTRACT

In this paper, a series of AlN–Al nanocomposite films are prepared by reactive magnetron sputtering. The effects of $N_2$ flow rate on the microstructure and mechanical properties of the films are studied. The formation and evolution mechanism of the nanocomposite structure are revealed. The results show that with the decrease of $N_2$ flow rate, the microstructure goes through three stages: pure AlN, amorphous Al surrounded nanocrystalline AlN and AlN nanoparticle reinforced Al matrix composite. Benefiting from the good wettability of Al on AlN ceramics, the film deposited at 6 sccm $N_2$ flow rate forms a nanocomposite structure of about 8 nm AlN grains wrapped by 1–2 nm amorphous Al. The hardness of the films increases first and then decreases with the decrease of $N_2$ flow rate, ranging from 4 GPa to 25 GPa. The toughness of the films is analyzed by the ratio of H/E, $H^3/E^2$, the normalized plastic depth ($\delta_H$) and the morphology of large load indentation. The results show that the toughness of the nanocomposite film obtained at 6 sccm $N_2$ flow rate is significantly improved while maintaining the hardness equivalent to that of pure AlN film. The improvement in toughness comes from the microcracks initiated in AlN hindered by the surrounding Al phase.

## 1. Introduction

Aluminum nitride ceramics (AlN) have received special attention due to their excellent properties such as high band gap, adjustable refractive index, high resistivity, high hardness and thermal stability. The combination of functional and hard film properties makes AlN more and more application in optical sensors [1–5], microelectronic devices [6,7], and wear-resistant coatings [8,9].

As a hard film, improving the mechanical properties of AlN has always been the direction of research. At present, the usual method is to introduce heterolayers to form superlattice structures or add other elements to form nanocomposite structures. Since the mechanical properties of superlattice films are heavily dependent on their modulation period, it is difficult to apply in industrial production. In contrast, nanocomposite is an effective way to improve the performance of AlN film. By adding Cr [10], Ti [11], Si [12] and other elements to form a composite film, the hardness and wear resistance of AlN film can be significantly improved. However, excellent wear resistance not only requires high hardness, but also good toughness. Musil et al. [13] proposed an nc-MeN/soft metal nanocomposite structure in which nanocrystalline MeN is wrapped with a thin layer of soft metal. The propagation of microcracks in MeN ceramics is inhibited by the outer soft metal layer, which significantly improves the toughness of the film. Similar results have been reported in TiN/Cu [14], ZrN/Cu [15], ZrN/Ag [16], $TiB_2$/Ni [17] and other systems.

The similar attempts have been made in AlN-based hard films, but they are not easy to succeed. Most of the added soft metals are agglomerated individually, rather than wrapped around AlN nanocrystalline. For example, Figueiredo et al. [18] prepared AlN/Au composite films with Au content of 0–2.5 at.% by magnetron sputtering. The Au element is embedded in the AlN matrix in the form of small particles. Domingues et al. [19] observed the same phenomenon in AlN/Cu, AlN/Ag, and AlN/Au systems. Guo et al. [20] even detected the formation of Al–Cu compounds in the AlN/Cu system. The above studies show that selecting the right soft metal for AlN-based films is the key to forming nanocomposite structures.

In this paper, the AlN/Al system is selected as the research object. A series of AlN/Al nanocomposite films are prepared by reactive magnetron sputtering. The mechanical behavior of films is studied, and the formation mechanism of nanocomposite structures is revealed.

* Corresponding author.
*E-mail address:* shanghl@sdju.edu.cn (H. Shang).

https://doi.org/10.1016/j.ceramint.2023.11.276
Received 6 June 2023; Received in revised form 22 October 2023; Accepted 22 November 2023
Available online 25 November 2023

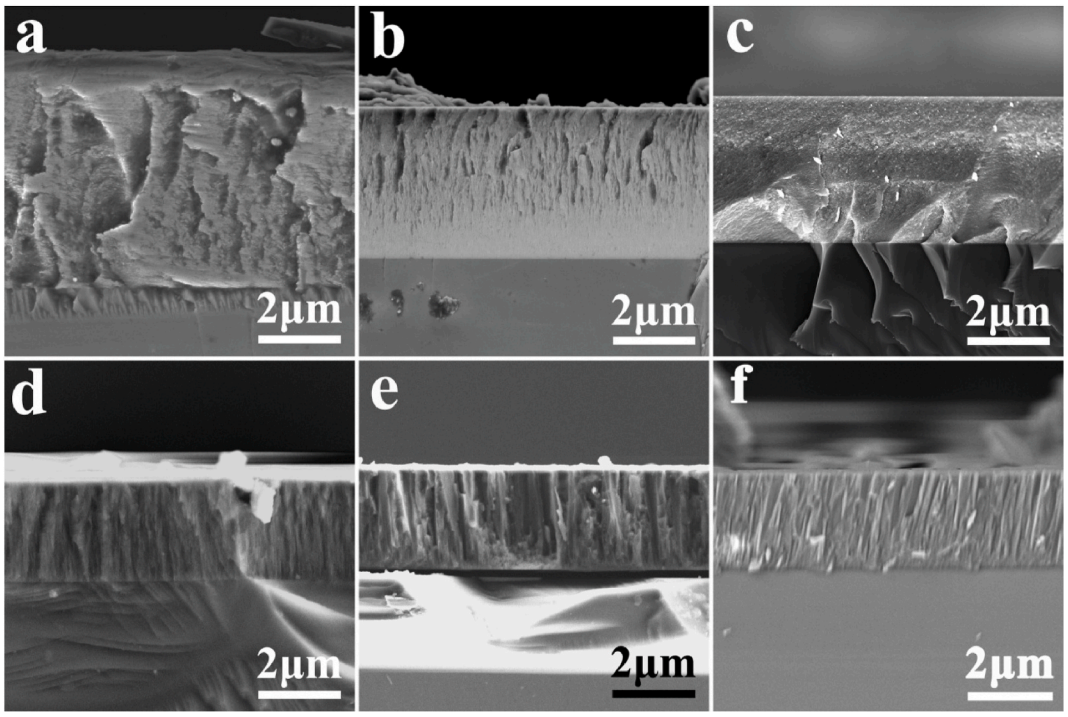


**Fig. 1.** Cross-sectional SEM images of AlN–Al nanocomposite films at different $N_2$ flow rate (a) 0 sccm, (b) 2 sccm, (c) 4 sccm, (d) 6 sccm, (e) 8 sccm, (f) 10 sccm.

## 2. Experimental

### 2.1. Film preparation

The AlN–Al nanocomposite structure films in this paper are prepared by ANAVA SPC-350 magnetron sputtering system. The substrate is monocrystalline silicon wafer. The Si substrates are ultrasonically washed in acetone and alcohol for 15 min, dried and fixed on a substrate rack in the chamber. The chamber is vacuumed to $5.0 \times 10^{-4}$, and then filled with high-purity argon (99.99 %) and nitrogen (99.99 %). The pure Al target (99.99 %) with a diameter of 76 mm is controlled by an RF cathode. During the deposition process, the working pressure of the chamber is fixed at 0.6 Pa, and the power of the RF Al target is controlled at 150 W. By selecting the $N_2$ flow rates of 0, 2, 4, 6, 8, 10 sccm respectively, a series of AlN–Al nanocomposite structure films are prepared. The substrate is not heated or negatively biased during the deposition process.

### 2.2. Film characterization

The Bruker's D8 X-ray diffraction (XRD) with Cu Kα target is used to analyze the phase composition of thin films. The 2θ angle ranges from 30 to 60°. The chemical bonds of the films were investigated using X-ray photoelectron spectroscopy (XPS, ESCALAB250XI, Thermo Fisher, USA) with Al Kα irradiation at a pass energy of 160 eV. The microstructure of the films is analyzed by JEOL JEM-2100F transmission electron microscopy. The cross-sectional morphology and thickness of the films are observed and measured by ZEISS' Gemini300 field emission scanning electron microscope. Anton Paar's Step300-$NTH_3$ nanoindenter is used to measure the mechanical properties of the films. The maximum load is 10 mN, both the loading and unloading time are all 20 s, and the holding time is 10 s. The loading and unloading curves are analyzed by the Oliver-Pharr method [21] to obtain the hardness and elastic modulus information of the film. Each sample is averaged after measuring at least 10 points to ensure the accuracy of the test results. The indentation tests with 200 mN are also performed using this nanoindenter. The plan-view morphology of indentation is characterized by an optical microscope attached to the nanoindenter. The cross-sectional samples of the indentation are prepared by the Hitachi IM4000Plus ion milling system. The ZEISS Gemini300 field emission scanning electron microscope is used to analyze the cross-section morphology of the indentation.

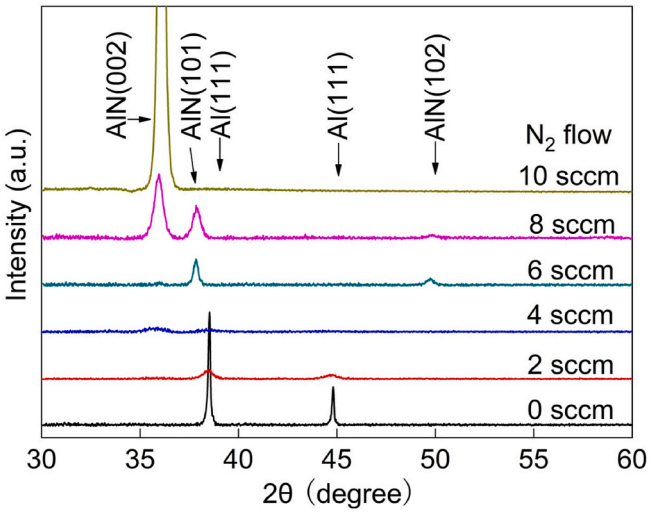


**Fig. 2.** XRD pattern of AlN–Al composite film.

## 3. Results

### 3.1. Microstructure

Fig. 1 shows the cross-sectional SEM image of AlN–Al nanocomposite films obtained at different $N_2$ flow rates. In this figure, the thickness of the composite film gradually decreases with the increase of $N_2$ flow rate, from 5.6 μm at 0 sccm to 2.3 μm at 10 sccm. The analysis of fracture morphology shows that the fracture of the film at 0 sccm and 2 sccm is a ductile fracture. There are many dimples in the fracture and the dimples

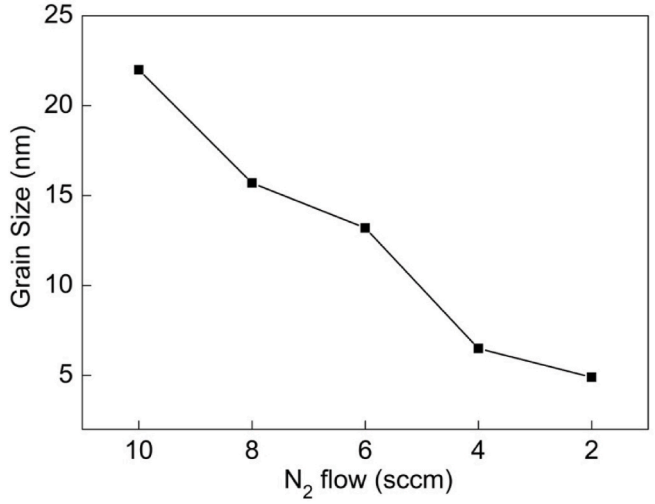


**Fig. 3.** Variation of grain size of AlN–Al composite films with $N_2$ flow rates.

of the film at 2 sccm are finer. When the $N_2$ flow rate is 4 sccm, the fracture is flat and smooth, showing obvious brittle fracture morphology. The film fractures with 6 sccm, 8 sccm and 10 sccm $N_2$ flow rates show obvious columnar crystal brittle fracture morphology.

Fig. 2 shows the XRD pattern of each AlN–Al composite film. There are only one strong AlN (002) diffraction peak in the film obtained at 10 sccm $N_2$ flow rate, indicating a preferential orientation growth on the (002) plane. When the $N_2$ flow rate decreases to 8 sccm, the intensity of the AlN (002) diffraction peak significantly decreases, while the (101) and (102) diffraction peaks of AlN appeared. When the $N_2$ flow rate further decreased to 6 sccm, the peak intensities of three diffraction peaks decreased, indicating that the crystalline perfection of the film has been disrupted. When the $N_2$ flow rate decreased to 4 sccm, a weak Al (111) diffraction peak appeared in the film, and AlN only has one diffuse (002) diffraction peak left. This indicates the formation of a microstructure in which nanocrystalline AlN and Al coexist in this film. After further reducing $N_2$ flow rate, the Al (111) diffraction peak significantly increased, accompanied by the appearance of the Al (200) peak. The diffraction peak of AlN (002) becomes even weaker. This indicates that the Al phase content in the film increases, while the AlN phase decreases.

Fig. 3 shows the variation of film grain size with $N_2$ flow rate. The grain size is calculated using the Scheler formula based on the information of AlN (002) diffraction peaks in the XRD results of Fig. 2. As shown in the figure, the grain size of the thin film gradually decreases with the decrease of $N_2$ flow rate, from about 22 nm at 10 sccm to about 5 nm at 2 sccm.

In order to study the existence form of Al in AlN–Al composite films, we conducted XPS analysis on films with different $N_2$ flow rates. The results are shown in Fig. 4. The survey spectrum in Fig. 4a indicates the presence of O 1s, N 1s, and Al 2p peaks in the film. The binding energy corresponding to the Al 2p peak is shown in Fig. 4b, wherein the broad peak associated with Al $2p_{3/2}$ are all centered at 74 eV and maybe decoupled into three peaks: the first one centered at 74.8 eV, referring to Al–O [22]; the second one centered at 73.9 eV, referring to Al–N [23]; the third one centered at 72.8 eV, referring to Al-Al [24]. When the $N_2$ flow rate is 10 sccm, the peak of the Al–Al bond is very weak, indicating that there is very little elemental Al in the film. As the $N_2$ flow rate decreases, the peak strength of the Al–N bond gradually decreases, while the peak strength of the Al–Al bond increases, indicating that the elemental Al content in the film gradually increases.

In order to further analyze the microstructure of the film, the TEM analysis is performed on AlN–Al composite films prepared at $N_2$ flow rates of 10 sccm and 6 sccm, as shown in Fig. 5. The bright field image in Fig. 5a shows that the film prepared at 10 sccm has fine and uniform grains. The upper right corner is the SAED spectrum of the film. A bright and three very weak diffraction rings can be observed in the figure, which corresponding to the AlN (002), Al (102), (110), and (200) crystal planes, respectively. By selecting the AlN (002) diffraction ring for dark field analysis, TEM dark field images of the corresponding region can be obtained, as shown in Fig. 5b. In this figure, the grain size of the film is approximately 15–20 nm. The film obtained at 6 sccm $N_2$ flow rate exhibits completely different microstructures. From the TEM bright field image in Fig. 5c, it can be seen that the film forms a two-phase structure with light bands surrounding dark particles. The TEM high-resolution image (Fig. 5d) can be obtained by local enlargement of Fig. 5c. It can be determined that the dark particles are AlN nanocrystalline by measuring the spacing of the lattice fringes. Its grain size is only about 5–8 nm. The light-colored banded structure wrapping the AlN nanocrystals is the Al phase. This is because as the $N_2$ flow rate decreases, there is not enough N to combine with Al atoms to form AlN during the deposition process, which ultimately leads to excessive Al. The excess Al will be enriched at the interface of AlN grains. Since the SAED pattern in the upper right corner of Fig. 5c shows only one AlN (101) diffraction ring without any Al diffraction ring, the Al phase is amorphous structure. Its thickness is about 1–2 nm. Therefore, a nanocomposite structure of amorphous Al (a-Al) surrounding nanocrystalline AlN (nc-AlN) is formed in this film.

Fig. 6 shows a cross-sectional TEM photo of the film at 6 sccm. As shown in Fig. 6a, the film exhibits an extremely fine columnar crystal structure. In order to observe the cross-sectional morphology more clearly, we conducted HRTEM analysis on this sample (Fig. 6b). Due to the extremely small AlN columnar crystals in this film, even in the thin

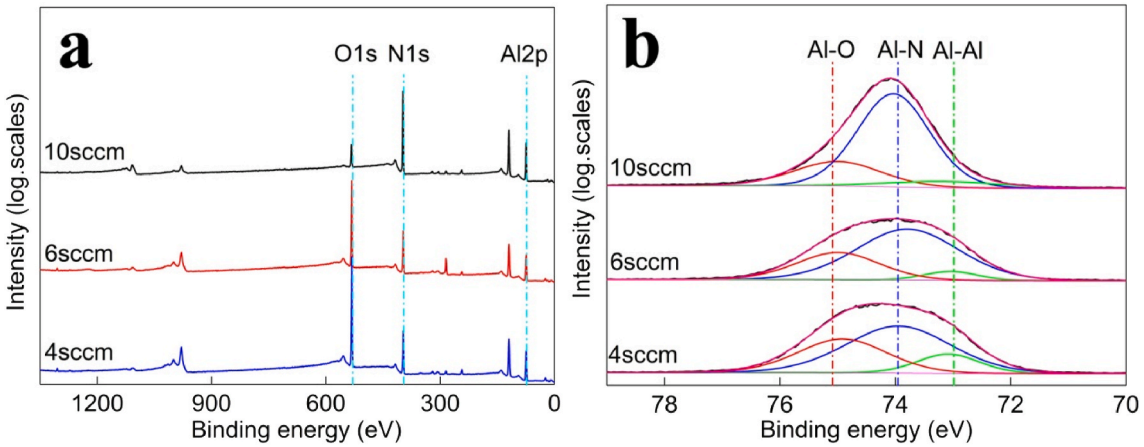


**Fig. 4.** XPS survey scan (a) and XPS spectra of Al 2p energy regions (b) for the AlN–Al films deposited at different $N_2$ flow.

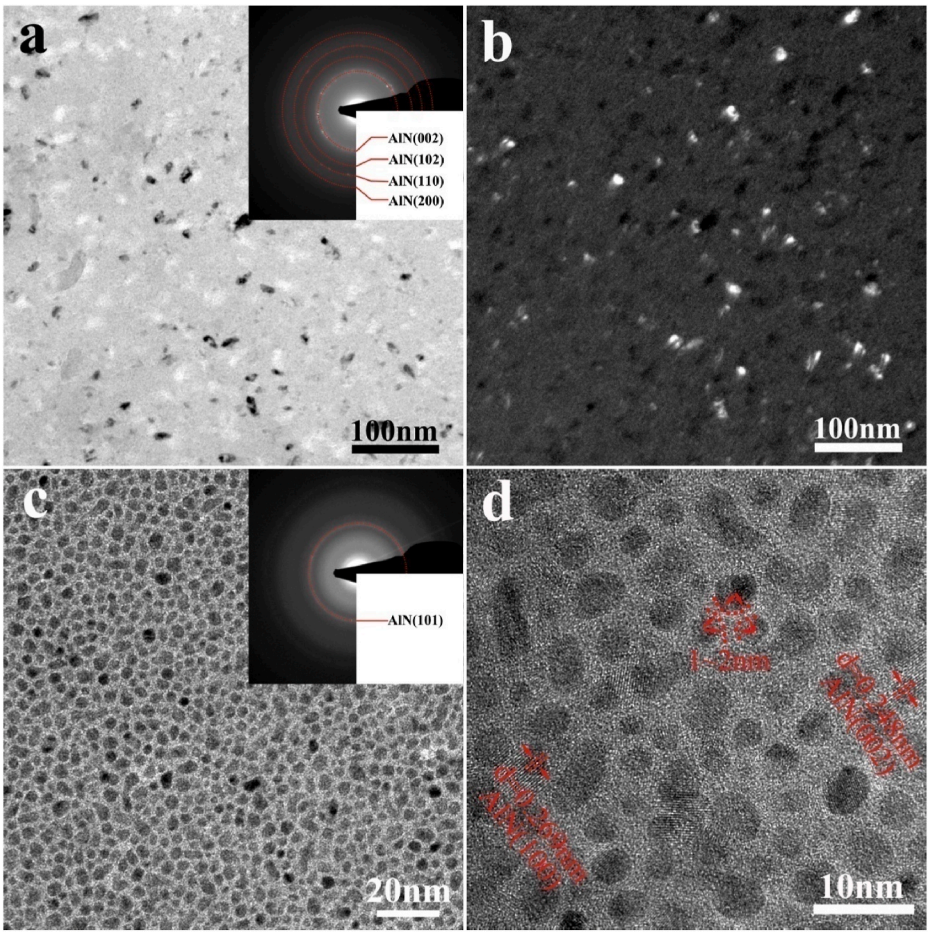


**Fig. 5.** TEM images of AlN–Al composite films at 10 sccm (a, b) and 6 sccm (c, d) $N_2$ flow rates.

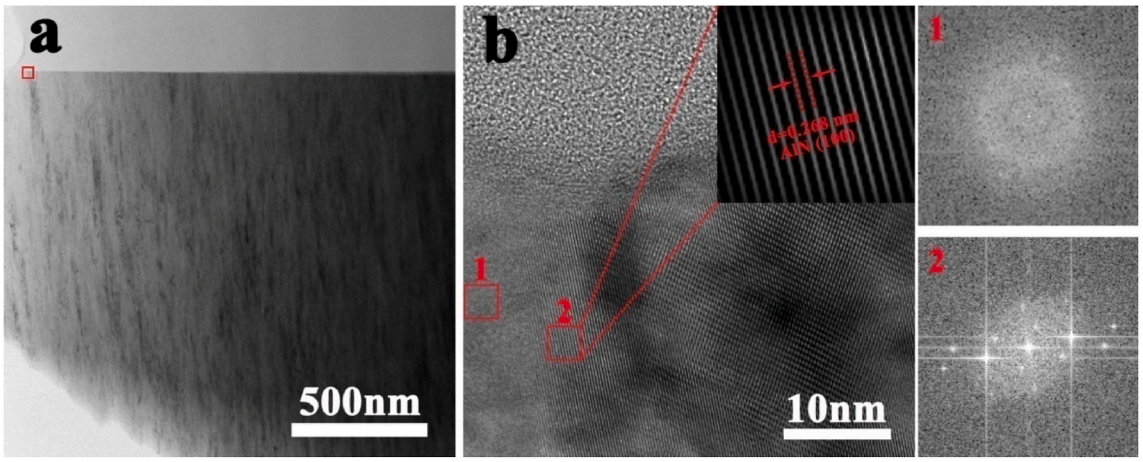


**Fig. 6.** Cross-sectional TEM images (a) and high-resolution images (b) of AlN–Al composite film at 6 sccm $N_2$ flow rate.

area of the TEM sample, there may be several AlN grains overlapping with each other. To avoid this impact, we selected the area as thin as possible area for HRTEM analysis (the red box in Fig. 6a), and the results are shown in Fig. 6b. The electron diffraction patterns obtained from Fourier transform indicate that the red box area 2 in Fig. 6b shows a clear crystal structure. The measurement results indicate that the lattice spacing is 0.268 nm, corresponding to the (100) crystal plane of AlN. The electron diffraction pattern in the red box 1 area presents an amorphous structure, indicating that the thin film forms a structure of amorphous Al surrounding nanocrystalline AlN. This result is consistent with the plan-view TEM results in Fig. 5.

### 3.2. Mechanical properties

Fig. 7 shows the variation of hardness and elastic modulus of AlN–Al composite film with $N_2$ flow rate. When the flow rate of $N_2$ is 10 sccm, the hardness of the film is 23.7 GPa. With the decrease of $N_2$ flow rate, the film hardness increased first and then decreased, and reaches a

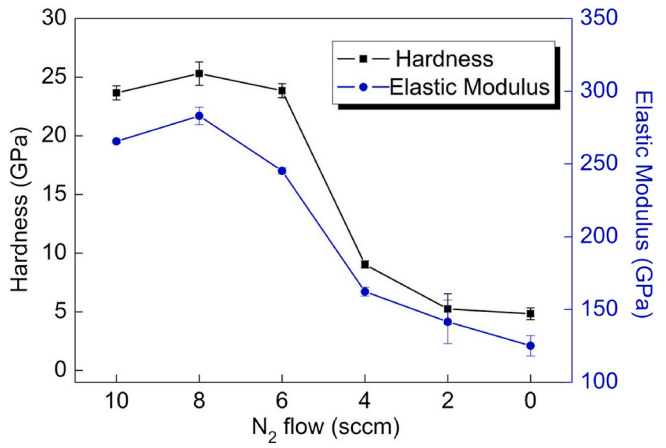


**Fig. 7.** Variation of hardness and elastic modulus of AlN–Al composite films with $N_2$ flow rates.

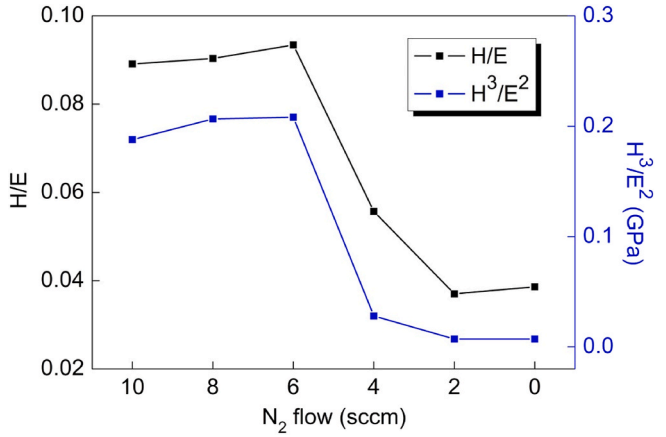


**Fig. 8.** Variation of H/E and $H^3/E^2$ of AlN–Al composite films with $N_2$ flow rates.

maximum of 25.3 GPa at 8 sccm $N_2$ flow rate. When the $N_2$ flow rate is 6 sccm, the hardness of the film is slightly reduced to 23.8 GPa. When the $N_2$ flow rate is further reduced to 4 sccm, the hardness of the film significantly decreases. Combined with the XRD results in Fig. 2, it can be seen that the film forms a structure in which nanocrystalline AlN and nanocrystalline Al coexist. The appearance of crystalline Al phase is the main reason for the significant decrease in the film hardness. With the further decrease of $N_2$ flow rate, the content of Al phase in the film increases gradually, which leads to the continuous decrease of film hardness. In addition, the elastic modulus of the film also shows a similar trend with the hardness. The greater the ability, the greater the responsibility.

The previous studies have shown that the ratio of H/E and $H^3/E^2$ is considered to be a potential indicator of film fracture resistance. Musil and co-workers [25] reported H/E for various oxide and nitride films. The results show that there is a strong correlation between H/E and surface cracking in film indentation and bending. Generally, the higher the H/E ratio value, the better the cracking resistance. Pei and co-workers [26] study the effect of substrate bias on the properties of nc-TiC/a-C:H nanocomposite films. The results show that the film with the higher $H^3/E^2$ ratio has a larger critical load of radial cracking. Fig. 8 shows the H/E and $H^3/E^2$ ratios of the AlN–Al composite film at different $N_2$ flow rates. With the decrease of $N_2$ flow rate, the curves of the both ratios increase first and then decrease. The two ratios reach a maximum at 6 sccm $N_2$ flow rate and then decrease significantly. The change in the type of film structure is the main reason for the large decrease of the two ratios.

Fig. 9a shows the load-indentation depth curve of each film. The curves are generally distributed in two regions. The indentation depth of the films at 10-6 sccm is smaller, indicating that the hardness of the film is higher. The indentation depth of the films is larger at 4-0 sccm. The film is transformed from AlN-based to Al-based. In addition, the normalized plastic depth value, $\delta_H$, which can easy and quick to evaluate the plasticity of the film [27], is also be obtained from the load-indentation depth curve. $\delta_H = h_p/h_{max}$, where $h_p$ is the indentation depth that cannot be rebounded, and $h_{max}$ is the maximum indentation depth. In general, the higher the value of $\delta_H$, the better the toughness of the film. The calculated $\delta_H$ value of films are shown in Fig. 9b. With the decrease of $N_2$ flow rates, the $\delta_H$ value gradually increased, indicating that the toughness of the film is improved.

Fig. 10 shows the indentation morphology of each composite film under a load of 200 mN. When the $N_2$ flow rate is 10 sccm, the indentation edge is clear and sharp. There are cracks at the top of the indentation, which indicates that the film is brittle. There are no cracks around the indentation of the films obtained at 6 and 2 sccm $N_2$ flow rate, indicating an improvement of films toughness. The indentation of 2 sccm film is larger, which indicates that the hardness of the film is lower.

Fig. 11 shows the cross-sectional SEM morphology of the indentation of films obtained at 10 sccm (Fig. 11a) and 6 sccm (Fig. 11b) $N_2$ flow rates. The load is 200 mN. Fig. 11a shows that cracking occurred on the surface of the film at 10 sccm. The cracks extend in multiple directions, dividing the thin film into fragments with different sizes. This indicates that the film is relatively brittle. Due to the severe fragmentation of the film, it is difficult to observe the complete indentation morphology in Fig. 11a. In comparison, the film at 6 sccm exhibit completely different

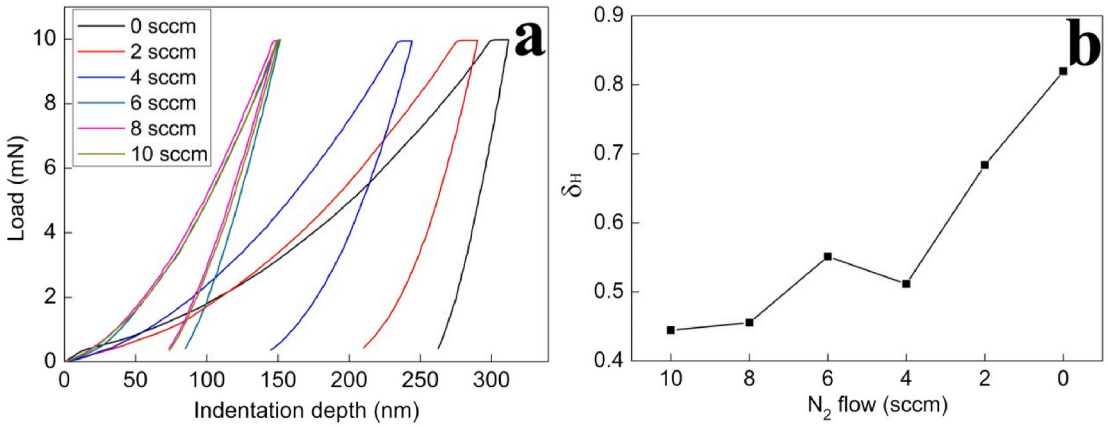


**Fig. 9.** Indentation curves and $\delta_H$ values of AlN–Al composite films at different $N_2$ flow rates.

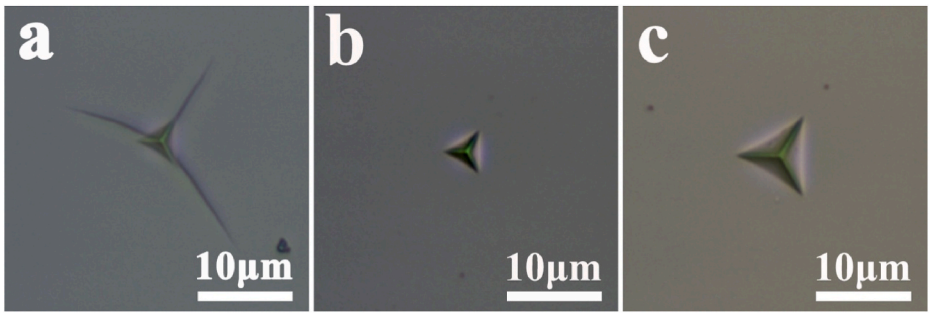


**Fig. 10.** OM images of indentation morphology of AlN–Al composite film at different $N_2$ flow rates (a) 10 sccm, (b) 6 sccm, (c) 2 sccm.

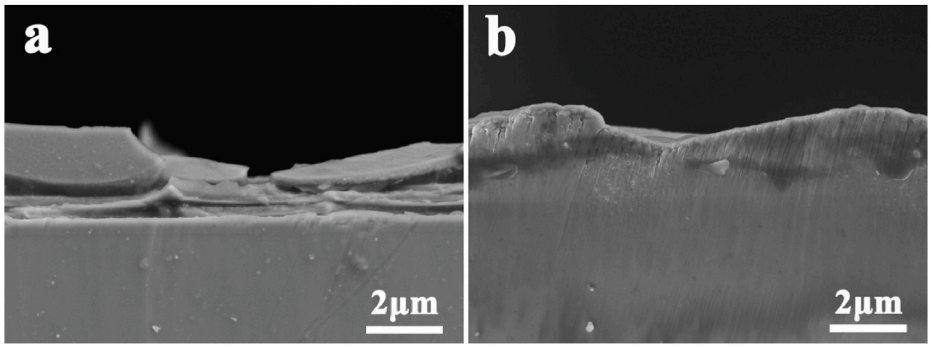


**Fig. 11.** The cross-sectional SEM morphology of the indentation of films obtained at 10 sccm (a) and 6 sccm (b) $N_2$ flow rates.

deformation behaviors. As shown in Fig. 11b, the indentation morphology of this film is clear and complete. There are no obvious cracks around the indentation, only protrusions appeared at the edge of the indentation. This indicates that this film has good toughness. These results are consistent with the OM photo of the indentation morphology in Fig. 10. Furthermore, it should be noted that both film fragmentation (Fig. 11a) and film deformation (Fig. 11b) caused by indentation occur inside the film. The substrate does not crack or deform. This indicates that the experimental results are not affected by the substrate.

## 4. Discussions

### 4.1. Microstructure evolution

Since Musil et al. [13] proposed the nc-MeN/soft metal structure, the nanocomposite film has attracted a lot of researches. However, it is not easy to obtain this structure. For example, Ju et al. [28] study the TiN–Ag system and found that when the Ag content was only 0.7 at.%, Ag nanoparticles appeared in the composite film.When the content of Ag increases to 23.5 at.%, Ag particles enrich at the grain boundaries of TiN nanocrystals. The similar phenomena also appear in AlN–Ag [18], AlN–Au [19] and other systems. In the study of $TiB_2$–Ni system, Wang et al. [17] found that when the Ni content is 10.8 at.%, the film forms composite structure of Ni surrounding nanocrystalline $TiB_2$ in the film. It can be seen that the choice of system is very important for the formation of nc-MeN/soft metal nanocomposite structure. The wettability study of the above systems shows that the contact angle of Ag to TiN at 1050 °C is 140° [29]. The AlN–Ag and AlN–Au [30] are also non-wetting systems. However, the contact angle of Ni to $TiB_2$ at 1500 °C can be lower than 50° [31]. These results indicate that good wettability is the key point for the formation of nc-MeN/soft metal nanocomposites.

In this paper, the AlN–Al film deposited at 6 sccm $N_2$ flow rate formed nc-AlN/a-Al nanocomposite structure, which depends on the good wettability of Al on AlN ceramics. Some studies [32] have shown that the AlN/Al system can change from non-wetting to wetting at temperatures above 850 °C. Zhang's research [33] shows that the essence of the wetting state transition is that the increase of temperature increases the kinetic energy of molten Al atoms. The high kinetic energy enables Al atoms to overcome the threshold for the formation of Al–N bonds with N atoms at the AlN surface. The states of Al atoms on AlN surface change from physical adsorption to chemical bonding, which improves the wettability of molten Al on AlN. The kinetic energy of Al atoms during magnetron sputtering is much higher than that of molten Al. The wettability of sputtered Al atoms to AlN will also be better. This is also confirmed by our previous work [34]. The high kinetic energy Al atoms can directly wet the AlN nanoparticles during the deposition process. The contact angle of molten Al on AlN ceramic is as low as about 30° at 700 °C. The excellent wettability is conducive to the formation of nc-AlN/Al nanocomposite structure in this paper.

### 4.2. Mechanical behavior

The research on ZrN–Cu composite film by Musil et al. [13] shows that the formation of nc-ZrN/Cu nanocomposite structure is accompanied by the appearance of superhardness. The highest hardness can reach more than 50 GPa. This phenomenon does not appear in the AlN–Al system in this paper. The hardness of the nc-AlN/a-Al nanocomposite film is only equivalent to that of the pure AlN film. This result is consistent with the study of $TiB_2$–Ni system by Wang [17]. The hardness of the nc-$TiB_2$/Ni nanocomposite film is basically the same as that of $TiB_2$, but the toughness is improved by more than 50 %. The potential reason for this result is that the Cu content in Musil's superhard ZrN–Cu nanocomposite films is very low, only 1–2 at.% Cu. The soft metal content in both our AlN–Al and Wang's $TiB_2$–Ni nanocomposite films exceeds 10 %. Although the excessive soft metal limits the improvement of the hardness, it greatly improves the toughness of the composite film.

Although increasing the ratios of H/E and $H^3/E^2$ can increase the toughness and wear resistance, it is difficult for hard films [35].That is because it is challenging to increase the film hardness without increasing the elastic modulus or to maintain the film hardness while decreasing the elastic modulus. Leyland et al. [36] suggests that adding soft metals

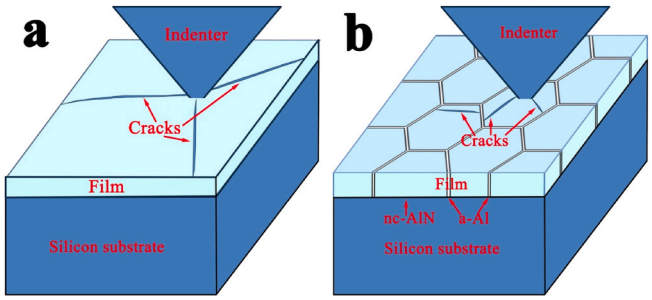


**Fig. 12.** The Schematic diagram of indentation experiments on AlN–Al composite films with different microstructures.

to hard films may be an effective approach. They doped Al into TiBN [37] to obtain TiAlBN nanocomposite films. The composite films obtain higher H/E and $H^3/E^2$ ratios than the TiBN films due to the reduction of the elastic modulus. The wear resistance of the composite film is improved by an order of magnitude due to the improvement of toughness. In this work, the hardness of the AlN–Al nanocomposite film obtained at 6 sccm $N_2$ flow rate is comparable to AlN film, while the ratios of H/E and $H^3/E^2$ are higher (Fig. 8). The indentation curves and $\delta_H$ values in Fig. 9 and the indentation morphology of Figs. 10 and 11 show that the toughness of this film is significantly improved. The above results confirm that the toughness of hard films is strongly correlated with the ratios of H/E and $H^3/E^2$, and also prove that the nanocomposite structure of nc-MeN/soft metal is an effective way to improve the ratios.

The previous studies [38] have shown that the improvement in toughness of nc-MeN/soft metal nanocomposite thin films comes from the suppression of microcrack propagation in MeN nanocrystals by ductile metals. Based on this theory, the deformation behavior of AlN–Al composite film with different microstructures during indentation experiment is illustrated in Fig. 12. As shown in Fig. 12a, when the $N_2$ flow rate is high, a pure AlN ceramic film will be formed. During the process of the indenter pressing into the film, micro-cracks that initiate around the indentation rapidly expand into macro-cracks once they form. The film is generally brittle. The film in Fig. 12b forms a nanocomposite structure in which amorphous al surrounds nanocrystalline AlN. The microcracks initiated in AlN will be hindered by the surrounding soft ductile Al phase. It is difficult for micro-cracks to grow into macro-cracks due to passivation [39], deflection [40]. The toughness of the film is greatly improved. The AlN grains in nc-AlN/a-Al composite structure prepared in this paper are very fine. During the indentation process, these fine AlN grains may even rotate, which makes the film have certain plastic deformation ability.

## 5. Conclusions

In this paper, a series of AlN–Al nanocomposite films are prepared by reactive magnetron sputtering. The effects of $N_2$ flow rate on the microstructure and mechanical properties of the films are investigated. The conclusions are as follows:

1 The grain size of the films decreased with the decrease of $N_2$ flow rate. When the $N_2$ flow rate is 6 sccm, the film forms a nanocomposite structure of nanocrystalline AlN with a diameter of about 8 nm surrounded by amorphous Al with a thickness of 1–2 nm. When the $N_2$ flow rate is further reduced, the film is gradually transformed into an Al-based composite reinforced by AlN particles.

2 With the decrease of $N_2$ flow rate, the hardness of AlN–Al nanocomposite films can be divided into two stages. When the $N_2$ flow rate is 10-6 sccm, the hardness of the film maintains at a high level of 23–25 GPa. When the $N_2$ flow rate is reduced to 4 sccm, the hardness of the film decreases sharply to below 10 GPa and continues to decrease with the further decrease of the $N_2$ flow rate.

3 The toughness analysis shows that the nanocomposite films obtained at 6 sccm have a significant improvement in all toughness indexes while keeping the hardness basically equal to that of AlN films. The improvement in toughness comes from the microcracks initiated in AlN hindered by the surrounding Al phase.

## Declaration of competing interest

The authors declare that they have no known competing financial interests or personal relationships that could have appeared to influence the work reported in this paper.

## Acknowledgements

The authors gratefully acknowledge the financial supports from the National Natural Science Foundation of China (No.52002240). CEMMPRE ref. “UIDB/00285/2020” and LA/P/0112/2020 projects, sponsored by FEDER funds through the COMPETE Program Operational Program on Competitiveness Factors and by national funds through the FCT Foundation for Science and Technology, which are also acknowledged.

## References

[1] R. Lin, W. Zheng, L. Chen, Y. Zhu, M. Xu, X. Ouyang, F. Huang, X-ray radiation excited ultralong (>20,000 seconds) intrinsic phosphorescence in aluminum nitride single-crystal scintillators, Nat. Commun. 11 (1) (2020) 4351, https://doi.org/10.1038/s41467-020-18221-1.
[2] Y. Zhu, R. Lin, W. Zheng, J. Ran, F. Huang, Near vacuum-ultraviolet aperiodic oscillation emission of AlN films, Sci. Bull. 65 (10) (2020) 827–831, https://doi.org/10.1016/j.scib.2020.02.018.
[3] J. Lin, Z. Wang, X. Lin, X. Wei, W. Zheng, Q. Hu, Amorphous-AlZnN/graphene heterostructure for solar-blind ultraviolet photovoltaic detectors, Ceram. Int. 49 (3) (2023) 4177–4183, https://doi.org/10.1016/j.ceramint.2022.09.300.
[4] R. Yu, G. Liu, G. Wang, C. Chen, M. Xu, H. Zhou, T. Wang, J. Yu, G. Zhao, L. Zhang, Ultrawide-bandgap semiconductor AlN crystals: growth and applications, J. Mater. Chem. C 9 (6) (2021) 1852–1873, https://doi.org/10.1039/D0TC04182C.
[5] Y. Zhang, J. Yang, D. Zhao, F. Liang, P. Chen, Z. Liu, High-quality AlN growth on flat sapphire at relatively low temperature by crystal island shape control method, Appl. Surf. Sci. 606 (2022), 154919, https://doi.org/10.1016/j.apsusc.2022.154919.
[6] L. Jia, F. Huang, W. Zheng, Vacuum ultraviolet (120–200 nm) avalanche photodetectors, Adv. Opt. Mater. 10 (8) (2022), 2102424, https://doi.org/10.1002/adom.202102424.
[7] W. Zhu, J. Hayden, F. He, J.-I. Yang, P. Tipsawat, M.D. Hossain, J.-P. Maria, S. Trolier-McKinstry, Strongly temperature dependent ferroelectric switching in AlN, $Al_{1-x}Sc_xN$, and $Al_{1-x}B_xN$ thin films, Appl. Phys. Lett. 119 (6) (2021), https://doi.org/10.1063/5.0057869.
[8] A. Bose, Soni, K. Singh, P. Dubey, S.K. Mishra, Study of dry sliding wear and corrosion behavior of nanocomposite Al-Si-N coated steel, Surf. Coat. Technol. 441 (2022), 128543, https://doi.org/10.1016/j.surfcoat.2022.128543.
[9] H. Mei, K. Yan, R. Wang, W. Peng, K. Huang, J. Shi, D. Zhang, W. Gong, F. Ren, Q. Wang, Microstructure and mechanical properties of nanomultilayered AlTiN/Cu coatings prepared by a hybrid system of AIP and PDCMS, Ceram. Int. 49 (1) (2023) 226–235, https://doi.org/10.1016/j.ceramint.2022.08.332.
[10] Z. Wu, F. Mei, W. Chen, Y. Yang, X. Lin, T. Yuan, J. Lin, Effects of the phase composition and grain size of Cr particles in Al–Cr targets on the microstructure and properties of AlCrN coatings, Ceram. Int. 48 (23) (2022) 35267–35279, https://doi.org/10.1016/j.ceramint.2022.08.129.
[11] J. Yi, S. Chen, K. Chen, Y. Xu, Q. Chen, C. Zhu, L. Liu, Effects of Ni content on microstructure, mechanical properties and Inconel 718 cutting performance of AlTiN-Ni nanocomposite coatings, Ceram. Int. 45 (1) (2019) 474–480, https://doi.org/10.1016/j.ceramint.2018.09.192.
[12] Soni, S.K. Sharma, S.K. Mishra, The effect of Si content on structural, mechanical and optical behaviour of magnetron sputtered Al–Si–N nanocomposite thin films, J. Alloys Compd. 831 (2020), 154686, https://doi.org/10.1016/j.jallcom.2020.154686.
[13] J. Musil, P. Zeman, H. Hrubý, P.H. Mayrhofer, ZrN/Cu nanocomposite film-a novel superhard material, Surf. Coat. Technol. 120–121 (1999) 179–183, https://doi.org/10.1016/S0257-8972(99)00482-X.
[14] Z.G. Li, S. Miyake, M. Kumagai, H. Saito, Y. Muramatsu, Hard nanocomposite Ti-Cu-N films prepared by d.c. reactive magnetron co-sputtering, Surf. Coat. Technol. 183 (1) (2004) 62–68, https://doi.org/10.1016/j.surfcoat.2003.09.051.
[15] P. Zeman, R. Čerstvý, P.H. Mayrhofer, C. Mitterer, J. Musil, Structure and properties of hard and superhard Zr-Cu-N nanocomposite coatings, Mater. Sci. Eng. A. 289 (1) (2000) 189–197, https://doi.org/10.1016/S0921-5093(00)00917-5.
[16] H. Ju, D. Yu, L. Yu, N. Ding, J. Xu, X. Zhang, Y. Zheng, L. Yang, X. He, The influence of Ag contents on the microstructure, mechanical and tribological

properties of ZrN-Ag films, Vacuum 148 (2018) 54–61, https://doi.org/10.1016/j.vacuum.2017.10.029.
[17] H. Wang, B. Wang, S. Li, Q. Xue, F. Huang, Toughening magnetron sputtered $TiB_2$ coatings by Ni addition, Surf. Coat. Technol. 232 (2013) 767–774, https://doi.org/10.1016/j.surfcoat.2013.06.094.
[18] N.M. Figueiredo, F. Vaz, L. Cunha, S.E. Rodil, A. Cavaleiro, Structural, chemical, optical and mechanical properties of Au doped AlN sputtered coatings, Surf. Coat. Technol. 255 (2014) 130–139, https://doi.org/10.1016/j.surfcoat.2014.03.028.
[19] R.P. Domingues, M.S. Rodrigues, C. Lopes, P. Pedrosa, E. Alves, N.P. Barradas, J. Borges, F. Vaz, Thin films composed of metal nanoparticles (Au, Ag, Cu) dispersed in AlN: the influence of composition and thermal annealing on the structure and plasmonic response, Thin Solid Films 676 (30) (2019) 12–25, https://doi.org/10.1016/j.tsf.2019.02.047.
[20] J. Guo, H. Wang, F. Meng, X. Liu, F. Huang, Tuning the H/E* ratio and E* of AlN coatings by copper addition, Surf. Coat. Technol. 228 (2013) 68–75, https://doi.org/10.1016/j.surfcoat.2013.04.008.
[21] W.C. Oliver, G.M. Pharr, An improved technique for determining hardness and elastic modulus using load and displacement sensing indentation experiments, J. Mater. Res. 7 (6) (2011) 1564–1583, https://doi.org/10.1557/JMR.1992.1564.
[22] S. Schoser, G. Brauchle, J. Forget, K. Kohlhof, T. Weber, J. Voigt, B. Rauschenbach, XPS investigation of AlN formation in aluminum alloys using plasma source ion implantation, Surf. Coating. Technol. 103–104 (1998) 222–226, https://doi.org/10.1016/S0257-8972(98)00397-1.
[23] G.F. Iriarte, J.G. Rodriguez, F. Calle, Synthesis of c-axis oriented AlN thin films on different substrates: a review, Mater. Res. Bull. 45 (2010) 1039–1045, https://doi.org/10.1016/j.materresbull.2010.05.035.
[24] M.H. Park, S.H. Kim, Thermal conductivity of AlN thin films deposited by RF magnetron sputtering, Mater. Sci. Semicond. Process. 15 (2012) 6–10, https://doi.org/10.1016/j.mssp.2011.04.007.
[25] J. Musil, M. Jirout, Toughness of hard nanostructured ceramic thin films, Surf. Coat. Technol. 201 (9) (2007) 5148–5152, https://doi.org/10.1016/j.surfcoat.2006.07.020.
[26] Y.T. Pei, D. Galvan, J.T.M. De Hosson, Nanostructure and properties of TiC/a-C:H composite coatings, Acta Mater. 53 (17) (2005) 4505–4521, https://doi.org/10.1016/j.actamat.2005.05.045.
[27] Y.V. Milman, B.A. Galanov, S.I. Chugunova, Plasticity characteristic obtained through hardness measurement, Acta Met. Mater. 41 (9) (1993) 2523–2532, https://doi.org/10.1016/0956-7151(93)90122-9.
[28] H. Ju, L. Yu, D. Yu, I. Asempah, J. Xu, Microstructure, mechanical and tribological properties of TiN-Ag films deposited by reactive magnetron sputtering, Vacuum 141 (2017) 82–88, https://doi.org/10.1016/j.vacuum.2017.03.026.
[29] P. Xiao, B. Derby, Wetting of titanium nitride and titanium carbide by liquid metals, Acta Mater. 44 (1) (1996) 307–314, https://doi.org/10.1016/1359-6454(95)00165-0.
[30] N.Y. Taranets, Y.V. Naidich, Wettability of aluminum nitride by molten metals, Powder Metall. Met. Ceram. 35 (5) (1996) 282–285, https://doi.org/10.1007/BF01328834.
[31] L. Xi, I. Kaban, R. Nowak, G. Bruzda, N. Sobczak, J. Eckert, Wetting, reactivity, and phase formation at interfaces between Ni–Al melts and $TiB_2$ ultrahigh-temperature ceramic, J. Am. Ceram. Soc. 101 (2) (2018) 911–918, https://doi.org/10.1111/jace.15188.
[32] H.-N. Ho, S.-T. Wu, The wettability of molten aluminum on sintered aluminum nitride substrate, Mater. Sci. Eng.A. 248 (1) (1998) 120–124, https://doi.org/10.1016/S0921-5093(98)00499-7.
[33] Q. Zhang, T. Cagin, A. van Duin, W.A. Goddard, Q. Yue, L.G. Hector, Adhesion and nonwetting-wetting transition in the Al/α-$Al_2O_3$ interface, Phys. Rev. B 69 (4) (2004) 1–11, https://doi.org/10.1103/PhysRevB.69.045423.
[34] Z. Ran, H. Shang, B. Ma, R. Li, F. Shangguan, D. Yu, Microstructure and mechanical properties of AlN/Al joints brazing by a sputtering Al/Cu bilayer film solder, Materials 15 (7) (2022) 2674, https://doi.org/10.3390/ma15072674.
[35] B.D. Beake, The influence of the H/E ratio on wear resistance of coating systems – insights from small-scale testing, Surf. Coat. Technol. 442 (2022), 128272, https://doi.org/10.1016/j.surfcoat.2022.128272.
[36] A. Leyland, A. Matthews, On the significance of the H/E ratio in wear control: a nanocomposite coating approach to optimised tribological behaviour, Wear 246 (1) (2000) 1–11, https://doi.org/10.1016/S0043-1648(00)00488-9.
[37] M.A. Baker, S. Klose, C. Rebholz, A. Leyland, A. Matthews, Evaluating the microstructure and performance of nanocomposite PVD TiAlBN coatings, Surf. Coat. Technol. 151–152 (2002) 338–343, https://doi.org/10.1016/S0257-8972(01)01657-7.
[38] S. Zhang, D. Sun, Y.Q. Fu, H.J. Du, Toughening of hard nanostructural thin films: a critical review, Surf. Coat. Technol. 198 (2005) 2–8, https://doi.org/10.1016/j.surfcoat.2004.10.020.
[39] M. Koyama, Z. Zhang, M. Wang, D. Ponge, D. Raabe, K. Tsuzaki, H. Noguchi, C. C. Tasan, Bone-like crack resistance in hierarchical metastable nanolaminate steels, Science 355 (6329) (2017) 1055–1057, https://doi.org/10.1126/science.aal2766.
[40] A. Pineau, A.A. Benzerga, T. Pardoen, Failure of metals I: brittle and ductile fracture, Acta Mater. 107 (2016) 424–483, https://doi.org/10.1016/j.actamat.2015.12.034.